Research Article Vol. 4, No. 5 / 15 May 2025 / Optics Continuum 1159
OPTICS CONTINUUM

# Concentric annular-hexagonal plasmonic resonator with nanorod vertices for dual-band absorption in NIR and MIR for sensing applications

AYON SARKER[1,2,3] AND SAJID MUHAIMIN CHOUDHURY[1,4]

[1]Department of Electrical and Electronic Engineering, Bangladesh University of Engineering and Technology, Dhaka, 1000 Dhaka, Bangladesh
[2]Department of Computer Science and Engineering, BRAC University, Dhaka, 1212 Dhaka, Bangladesh
[3]ayon.sarker@bracu.ac.bd
[4]sajid@eee.buet.ac.bd

**Abstract:** This study introduces a dual-band plasmonic absorber designed for simultaneous sensing applications in the near-infrared (NIR) and mid-infrared (MIR) regions. The absorber, composed of silver nanostructures on a metal plate with a dielectric spacer, exhibits a combination of localized and gap surface plasmon resonances, resulting in two distinct absorption peaks in the theoretical analysis conducted using numerical simulations. The two absorption peaks are located in the NIR band (1366 nm) and the MIR band (2683 nm), with impressive absorption rates of 99.5% and 99.99%, respectively. Numerical simulations further validate the sensor's high refractive index sensitivity of 1550 nm/RIU, enabling the detection of biomolecules, proteins, viruses, and various solutes in aqueous solutions. Along with the significant resonance shift, the absorber offers two working windows in distinct IR regions and the flexibility to select wavelengths in both bands simultaneously, thereby expanding its application range in environmental monitoring, medical diagnostics, and chemical sensing.



## 1. Introduction

The interest in plasmonics, an intriguing field that focuses on the interactions between free electron clouds in metallic structures and incoming photons [1], has surged significantly, leading to remarkable progress, especially in sensor technology [2,3]. Plasmonic absorbers have emerged as powerful tools in nanophotonics due to their extraordinary ability to confine electromagnetic (EM) waves at subwavelength scales, thereby facilitating enhanced light-matter interactions [4–6]. This capability has positioned them as a highly promising option for a range of applications, including bio-sensing, chemical sensing, gas sensing, biological analyte sensing, environmental and healthcare monitoring and sensing, photodetection, energy harvesting, and thermal emission [2,7–10]. Additionally, the combination of high sensing efficiency, cost-effectiveness, compact device size, stability, and the remarkable variety, accessibility, and reusability of optically functional materials has sparked significant interest in plasmon-based sensing technologies [11].

The driving principle behind plasmonic absorbers is surface plasmon resonance (SPR) [12], which refers to the excitation of surface plasmons that occurs when incident EM waves induce collective oscillations of free electrons at the metal-dielectric interface [13]. SPRs involve two fundamental types of electron oscillations triggered by incident EM radiation at metal-dielectric interfaces: surface plasmon polaritons (SPPs) and localized surface plasmons (LSPs) [14]. SPPs propagate along a conductor's surface, while LSPs, confined to metallic nanostructures, do not propagate but are closely coupled with the EM field. While LSPs can be excited directly by incidenting light, SPPs, on the other hand, require specific phase-matching techniques [15,16]. Due to their exceptional sensitivity to changes in the surrounding refractive index, refractive index

#558501 https://doi.org/10.1364/OPTCON.558501
Journal © 2025 Received 19 Feb 2025; revised 16 Apr 2025; accepted 17 Apr 2025; published 13 May 2025

OPTICS CONTINUUM

sensors based on both propagating surface plasmon resonance (PSPR) [17,18] and localized surface plasmon resonance (LSPR) [19,20] have been developed, each offering its advantages and limitations [21].

While LSPR sensors offer tunability based on nanoparticle size and shape [22], their sensitivity is generally lower than PSPR sensors [23]. However, to enhance sensor performance, a combination of these two modes can be utilized, particularly when using periodic nanoparticle arrays [23,24]. This is due to the energy transfer resulting from the enhanced electromagnetic coupling between LSP and PSP [25], which takes place when a metallic nanoparticle is in the close vicinity of a metallic surface through the interaction of dipoles within it and their mirror image on the metallic surface [26]. Moreover, the strength of interparticle coupling can be enhanced to a great extent by employing a periodic or quasi-periodic arrangement of nanoparticles (metasurfaces) instead of a single nanoparticle [27]. Another type of surface plasmon confinement, known as gap plasmon, occurs in the gap between two surfaces in a metal-insulator-metal (MIM) configuration—a 2D planar array supported by a metallic film with a thin spacer [28]. Combining these phenomena within a single setup provides superior control over reflected waves, enhances spectral selectivity, and enables nonlinear optical properties, all while maintaining a compact and streamlined device footprint [29,30].

Plasmonic absorbers are greatly admired, and researchers have been harnessing their advantages in the infrared (IR) region of the electromagnetic spectrum [31]. This is because IR light has a unique ability to resonate with most molecules due to the transition of molecular vibration and thus exhibits exceptional diffraction, penetration, and absorption properties [32], making this band essential for sensing and spectroscopy applications in medical, biotechnology, security, and defense fields [33]. The span of the IR spectrum is conventionally subdivided into three regions: near-infrared (NIR) (780–2500 nm); mid-infrared (MIR) (2500–25,000 nm); and far-infrared (FIR), which includes wavelengths beyond 25,000 nm [34]. NIR wavelengths are effective for detecting organic molecules, proteins, and proteinaceous structures [35], while MIR wavelengths are utilized mostly to identify specific molecular signatures [36]. Despite the numerous distinct conveniences that can be achieved in NIR and MIR bands individually, most reported IR absorbers have been limited to functioning within just one of these spectral ranges, which narrows their application scope and diminishes their potential effectiveness for a wide variety of sensing and detection tasks. Introducing the concept of developing dual-band plasmonic absorbers can offer a compelling solution to this limitation. By operating across different spectral regions, this type of plasmonic absorber can enhance its functionality and be capable of simultaneous detection of multiple analytes or even various properties of a single analyte. Multi-band sensors are highly suitable for biomedical applications due to their resolution and sensitivity accuracy [37], and they can be particularly valuable in applications requiring high sensitivity across diverse wavelengths, such as environmental monitoring, medical diagnostics, and chemical sensing. Therefore, researchers find designing multi-band sensors more appealing than developing single-band ones. Nevertheless, despite recent advancements in designing dual-band IR plasmonic absorbers for sensing, filtration, and characterization applications, most of their resonant frequencies still fall exclusively within either the NIR [38–40] or MIR [41–43] range, leaving the aforementioned concern unresolved.

Taking this issue into account, this study introduces a novel dual-band narrowband absorber consisting of arrays of silver nanostructures on a metal plate, with a layer of polymer separating them. The structure combines the effects of SPPs and LSPs, resulting in two absorption peaks: one at 1366 nm (219.5 THz, 7320.64 $cm^{-1}$) in the NIR region—specifically in the NIR-III range (1350 nm–1870 nm [44]). With these two absorption peaks, the design offers the benefits of dual working windows along with the versatility to choose preferred operating wavelengths in both the NIR and MIR regions at the same time for refractive index sensing applications. Additionally, the utilization of the NIR-III window enables applications in petroleum product analysis [45] and

OPTICS CONTINUUM

biological and biochemical detection [46,47]. Furthermore, the position of the second absorption peak in the MIR band, specifically within the "diagnostic or functional group region," can be used for the identification of molecular functional groups, such as amines, for applications in food safety, environmental monitoring, and biological sample analysis [34]. The simulation data from the numerical analysis of the proposed structure, using the finite-difference time-domain (FDTD) method, validate its ability to achieve dual resonances simultaneously and confirm its suitability as a plasmonic sensing platform, with the resonance being sensitive to the refractive index of the surrounding medium, the maximum refractive index sensitivity reaches 1550 nm/RIU. The compatibility of the sensor has been thoroughly examined through simulations for various applications, including the detection of gas hydrates in seawater, determining concentrations of solvents or the presence of biomolecules in aqueous solutions and organic fluids, detection of immobilized bio-layers, confirmation of DNA hybridization completion, etc. Due to its relatively simple structure and the compelling ability to operate simultaneously in two distinct regions of the IR spectrum, this absorber can be an attractive candidate for next-generation sensing technologies in medical diagnostics, environmental science, and chemical detection.

## 2. Structural composition and layout

The structure consists of three layers, starting with a metal plate at the base. A two-dimensional square array of metal nanostructure is deposited as the top layer on a sheet made of dielectric material that acts as a spacer between the top and bottom metal layers. The nano-structure is constructed with concentric annular-hexagonal plasmonic resonators with nanorod vertices as shown in Fig. 1(a). We used silver (Ag) to prepare the top layer of nanostructures and the metal plate at the bottom since it has significantly lower interband optical loss compared to other commonly used plasmonic metals like gold, aluminum, and copper [48]. The thickness of the Ag-nanostructures is 45 nm, and that of the silver plate at the base is 265 nm. We selected the thickness of the bottom plate to prevent any transmission of the incident light, taking into consideration the frequency-dependent skin depth of silver within the spectrum we are operating in [49]. A 90 nm thick layer of polymethyl methacrylate (PMMA) is incorporated on top of the silver layer as the dielectric spacer in this absorber. On top of this polymer layer, the square array of Ag-nanostructures is periodically repeated in the x and y directions. The Ag-nanostructures can be fabricated on the PMMA layer using the techniques reported previously [50,51]. Figure 1(b) shows a unit cell with a side length of P = 675 nm with a detailed view of the Ag-nanostructure. Each Ag-nanostructure contains a ring made of silver with inner radius $R_{IN}$ = 170 nm and outer radius $R_{OUT}$ = 210 nm. At the center of the ring, there is a hexagonal cuboid with a circumradius of $R_H$ = 80 nm. Lastly, we placed six Ag-nanorods with a diameter of 40 nm at the vertices of the hexagon. The locations of the centers of the nanorods arranged around the central hexagon are calculated such that the walls of the nanorods just make contact with the vertices of the hexagon. This is achieved by utilizing polar coordinates (with the origin at the center of the hexagon) and applying the following expressions (1), and (2),

$$r_n = R_H + \frac{D_{NR}}{2} \tag{1}$$

$$\theta_n = \frac{\pi}{3} \cdot n \tag{2}$$

where n = 0,1,2,3,4, and 5.

The square unit cell shown in Fig. 1(b) containing one Ag-nanostructure each on top of the PMMA layer, and a silver plate underneath, is two-dimensionally repeated to fabricate the entire layout of the proposed structure. Considering potential fabrication imperfections in Ag nanostructures, we analyzed the absorber's characteristics by shifting the radial coordinates of the nanorods' center from their actual position ($r_n$). In addition, we examined the structure's

OPTICS CONTINUUM

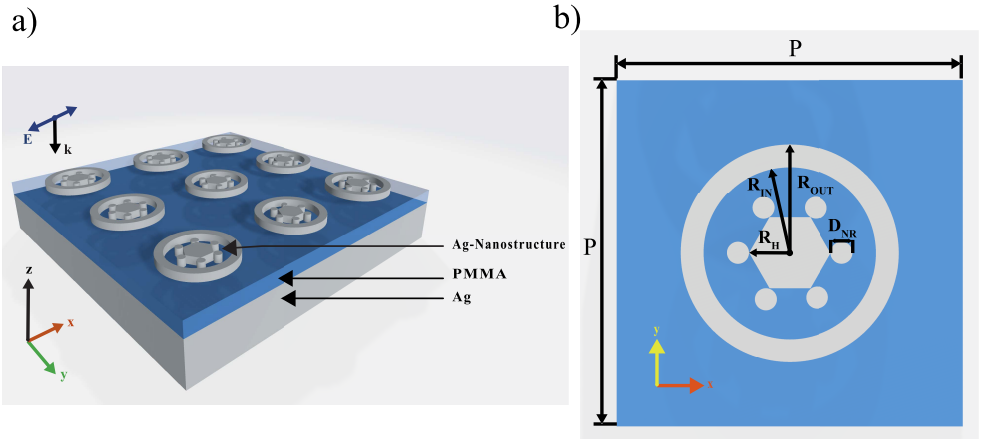


**Fig. 1.** a) Three-dimensional illustration of the proposed absorber, b) Orthographic top view of the unit cell.

response by introducing curvature at the hexagon vertices instead of sharp corners, as may also occur due to the aforementioned fabrication imperfections. Our findings indicate an acceptable tolerance range during fabrication (which will be discussed in detail in Fig. 5).

## 3. Methods

We simulated the proposed structure numerically by applying the three-dimensional FDTD method. To model our structure for the simulation, we employed the refractive index data of silver from [52], and for PMMA, using the Sellmeier model, we derived and utilized values calculated from the Eq. (3) below [53,54],

$$n^2 - 1 = \frac{0.99654\lambda^2}{\lambda^2 - 0.00787} + \frac{0.18964\lambda^2}{\lambda^2 - 0.02191} + \frac{0.00411\lambda^2}{\lambda^2 - 3.85727} \tag{3}$$

To obtain the absorption spectrum, we conducted simulations to calculate the reflection and transmission spectra by illuminating the absorber with a plane wave that is normally incident, propagating along the negative z-axis, and applying suitable boundary conditions along all three axes. In simulations periodic boundary conditions are imposed on all four sides of the structure in the x and y directions, while a perfectly matched layer (PML) absorption condition is applied to the top and bottom in the direction of the incident illumination. By analyzing absorption spectra computed with proper simulation settings for different applications, we also investigated the figure of merit (FOM), refractive index sensitivity, the full width at half maximum (FWHM), and other properties of the absorber we introduced in this work.

## 4. Result and discussion

The introduced absorber structure exhibits two absorption peaks when illuminated by light from a plane source. Utilizing the data from simulations, the absorption spectrum can be assessed using the expression A = 1-R-T, where R and T refer to reflection and transmission, respectively. Since the thickness of the silver plate at the base is chosen to be greater than its skin depth, the transmission is virtually zero all over the spectrum. From Fig. 2, it can be noticed that there are two dips in the reflection spectrum implying two absorption peaks—one at 1366 nm in the NIR-III range (Mode -1 or $M_1$) with 99.5% absorption (reflection 0.46%) and the second one at 2683 nm with 99.99% absorption in the MIR band (Mode-2 or $M_2$) (reflection 0.0051%).

OPTICS CONTINUUM

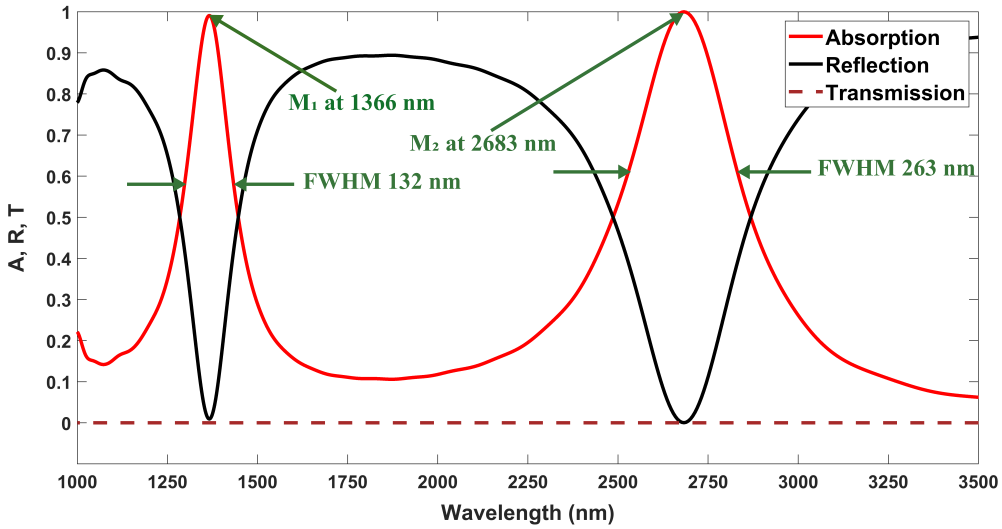


**Fig. 2.** Reflection, absorption, and transmission spectra of the proposed absorber for normally incident TM-polarized light with the electric field along the x-axis. The low transmission indicates high absorption at the resonant frequency, as A = 1 - R - T.

To explain the generation of two distinct absorption peaks, we analyzed two cases. First, for Ag nanostructures consisting of only a central hexagon and vertex nanorods, a peak $M_1$ at 1351 nm with 96% absorption, was observed. Next, for a structure with only the outer Ag ring, peak $M_2$ appeared at 2645 nm with 99% absorption. These results, as shown in Fig. 3, suggest that the inner hexagon and nanorods (inset of Fig. 3(a)) contribute to $M_1$, while the outer ring (inset of Fig. 3(b)) corresponds to $M_2$. The original structure, combining both, yields the absorption spectra as depicted in Fig. 2, where the positions of the peaks and the improved absorption (99.5% and 99.99%, respectively) for $M_1$ and $M_2$ are due to coupling between the inner structure and the outer ring through gap surface plasmon [55].

To investigate the underlying causes of the absorber's behavior at resonance frequencies, we thoroughly examined the electromagnetic field induced by the incident light within the absorber at two resonance wavelengths separately as shown in Fig. 4.

For $M_1$, Fig. 4(a) and (b) show the localized electric field that forms LSPR around the nanorods of the nanostructures on the topmost layer. The LSPR strongly couples to its mirror dipole on the bottom silver plate. In the case of $M_2$, as seen in Fig. 4(c), and (d) the electric field localizes at the outer and inner walls of the ring, and similarly couples to its dipole even more strongly than that for $M_1$. At both resonant frequencies, the gap surface plasmon can be noticed in the spacer layer of PMMA beneath the nanorods and ring, which is responsible for low reflectivity at resonant frequencies [55]. Additionally, the coupling between the inner structure and the outer ring through gap surface plasmon causes improved absorption (99.5% and 99.99%, respectively for $M_1$, and $M_2$) as discussed in Fig. 3. Furthermore, from Fig. 4(e), and (g) it can be observed that the induced magnetic field is concentrated at the hexagonal cuboid mainly in the Y direction for $M_1$, while for $M_2$, it is concentrated at the inner wall of the nanoring in the XY plane. Additionally, Fig. 3(f) and (h) show the intensity of the confined magnetic field along the YZ plane within the absorber for $M_1$ and $M_2$, respectively. The magnetic field induced by the incident light aids in the enhancement of the confined electromagnetic field, resulting in low reflectivity and, thereby, greater absorption [56]. In addition, the LSP mode of a single Ag nanostructure interacts with its adjacent Ag nanostructures in neighboring periodic unit cells through SPP, as shown in Fig. 4(i), leading to improved field confinement and enhanced absorption at the resonant frequency.

OPTICS CONTINUUM

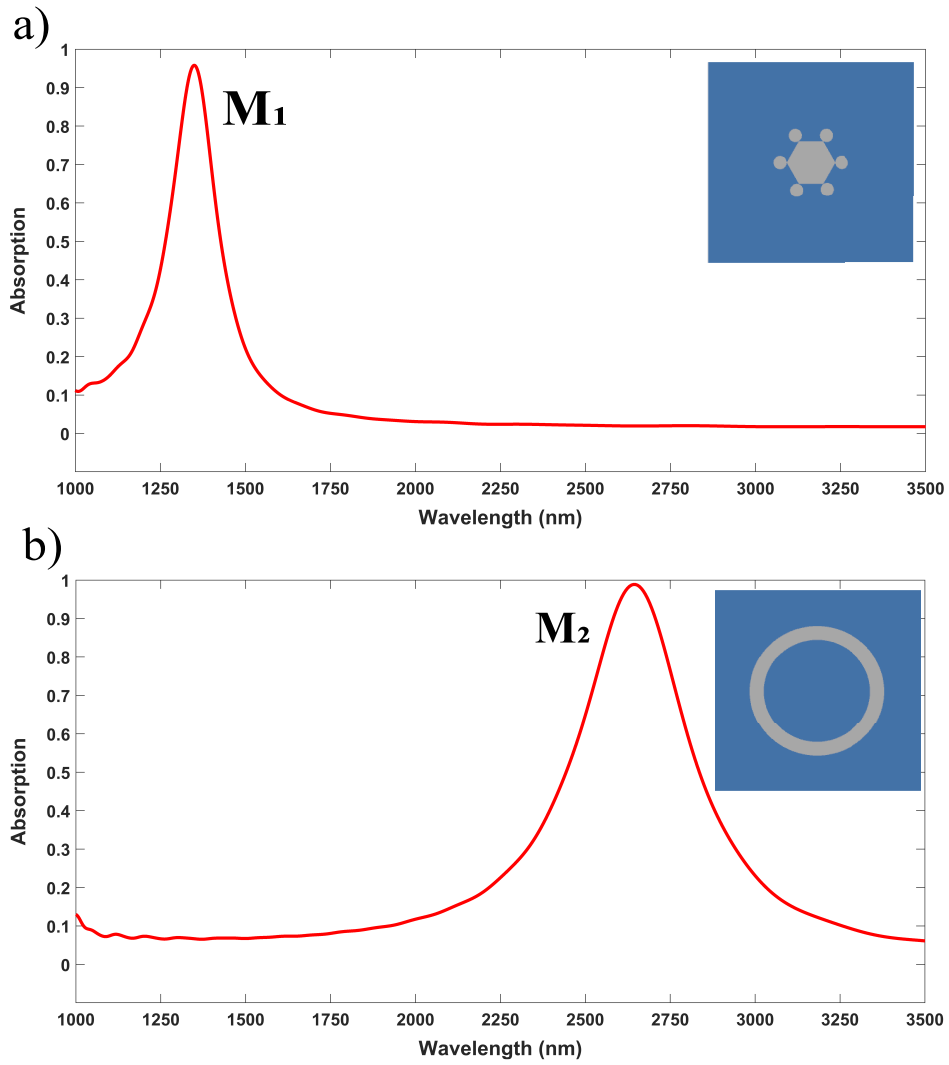


**Fig. 3.** Ag nanostructures correspond to the generation of absorption spectra a) $M_1$, b)$M_2$. The inset shows the schematic of the Ag nanostructure.

OPTICS CONTINUUM

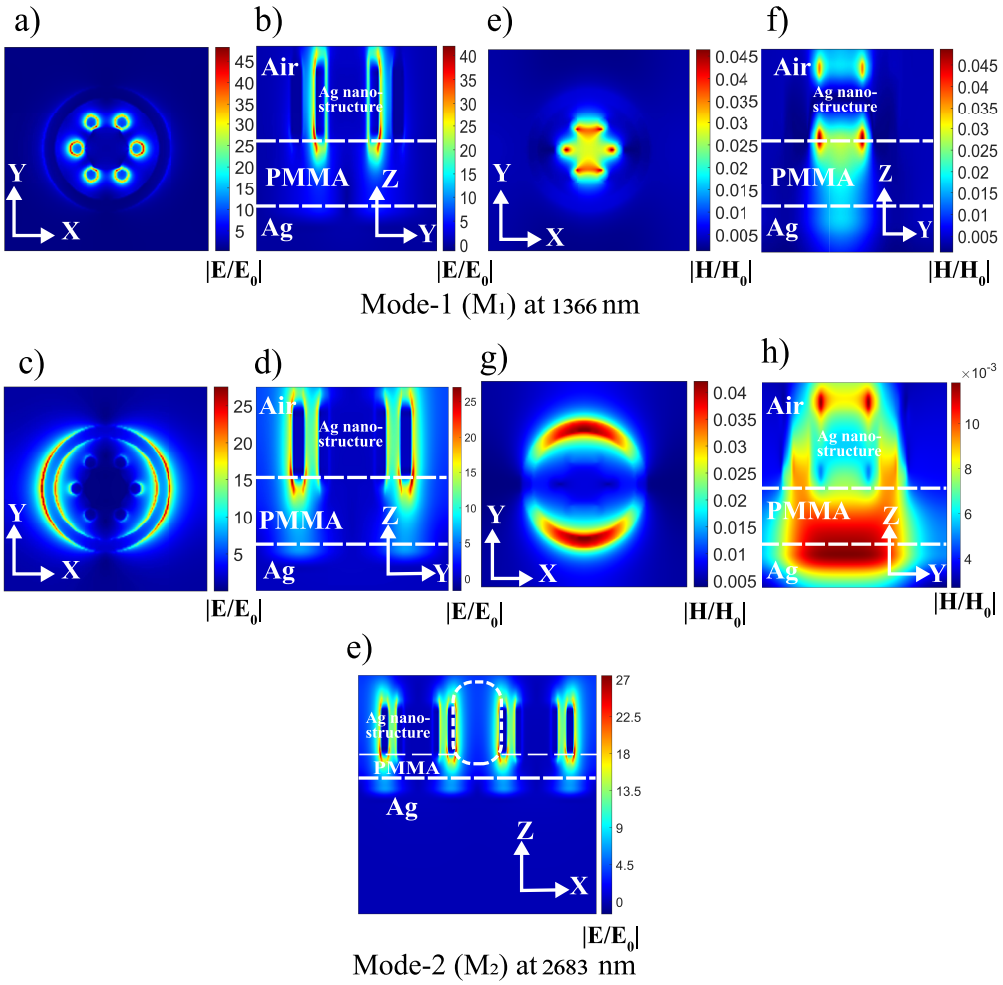


**Fig. 4.** Electric and magnetic field distributions for modes M1 and M2: (a, b) Electric field distribution for M1 at the a) XY and b) YZ cross-sections; (c, d) Electric field distribution for M2 at the c) XY and d) YZ cross-sections; (e, f) Magnetic field distribution for M1 at the e) XY and f) YZ cross-sections; (g, h) Magnetic field distribution for M2 at the g) XY and h) YZ cross-sections; (i) Field coupling between adjacent unit cells' Ag-nanostructures for M2 at the ZX cross-section (region marked by the dashed oval).

OPTICS CONTINUUM

Figure 5 shows the impact of slight positional deviations of nanorods at the central hexagon vertices, which may be introduced due to fabrication imperfections. The absorption spectra were calculated by altering the nanorods' radial coordinates to $r_n + d$, where $d$ denotes the deviation from the actual $r_n$ in Eq. (1). The results suggest an acceptable fabrication tolerance as the resonance peaks and absorption change minimally within this deviation range. However, as the separation between nanorods and hexagon vertices increases, the coupling between nanorods and the central hexagon weakens, reducing absorption for $M_1$ (e.g., when $r_n + d$=108 nm, absorption for $M_1$ drops to 95.5%). When $r_n + d$ is greater than 110 nm, the coupling vanishes, leaving only $M_2$. It can be observed that the deviation in the position of the nanorods has no effect on $M_2$, as this mode is generated due to the outer ring of the Ag nanostructure (as discussed in Fig. 3 and Fig. 4). Along with deviations in nanorod positions, we also considered possible imperfections in the hexagon shape due to fabrication. Since sharp corners are hard to achieve in metal structures, we analyzed the design's response with vertex curvatures of 15–30 nm instead of sharp points, using nanorods at $r_n + d$= 108 nm (see Supplement 1). This range reflects typical fabrication variations. The results show minimal impact on absorption (e.g., $M_1$ drops slightly to 95.2%, $M_2$unaffected), indicating the structure's tolerance to this imperfection. In practice, after fabrication, the imperfections in the structure can be examined using widely available scanning electron microscopes and characterized by analyzing the resonance wavelengths of $M_1$ and $M_2$ before any sensing application.

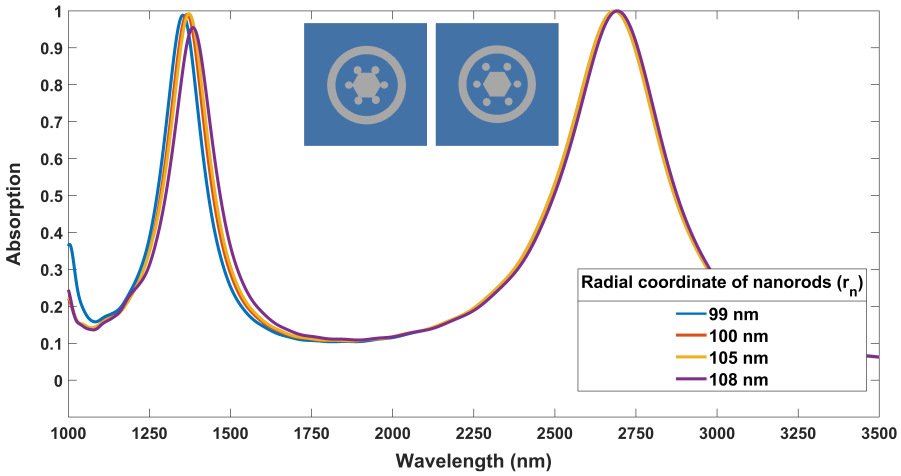


**Fig. 5.** Effect of nanorods' center deviation ($r_n + d$) from the expected position ($r_n$). The inset shows structures with $r_n + d$ = 99 nm (left), and with $r_n + d$ = 108 nm (right).

To examine the impact of geometric parameters of the introduced Ag-nanostructure, first, we varied the diameter of the nanorods ($D_{NR}$). With the increasing diameter of nanorods ($D_{NR}$), a redshift in both resonance wavelengths can be noticed in Fig. 6(a). The change in diameter of nanorods ($D_{NR}$) affects the position of the $M_1$ more since the resonance at $M_1$ is essentially associated with the nanorods as noticed from Fig. 4(a). Figure 6(b), and (c) show the consequence of the change in the inner and outer radii ($R_{IN}$ and $R_{OUT}$) of the nanoring. Since it is seen in Fig. 4(c) that the resonance at $M_2$ is linked to both the inner and outer walls of the ring, changes in the radii primarily influence the position of the $M_2$ resonance. However, as the inner radius of the ring ($R_{IN}$) increases, the field coupling between the inner wall of the ring and the nanorods becomes less strong due to the expanding gap between them, resulting in lower absorption and shifts in the positions of both $M_1$ and $M_2$. Alternatively, adjusting the outer radius of the ring

OPTICS CONTINUUM

($R_{OUT}$) has minimal to no effect on the position of $M_1$. However, as the width of the ring varies, both the absorption rate and the position of $M_2$ change, as shown in Fig. 6(c).

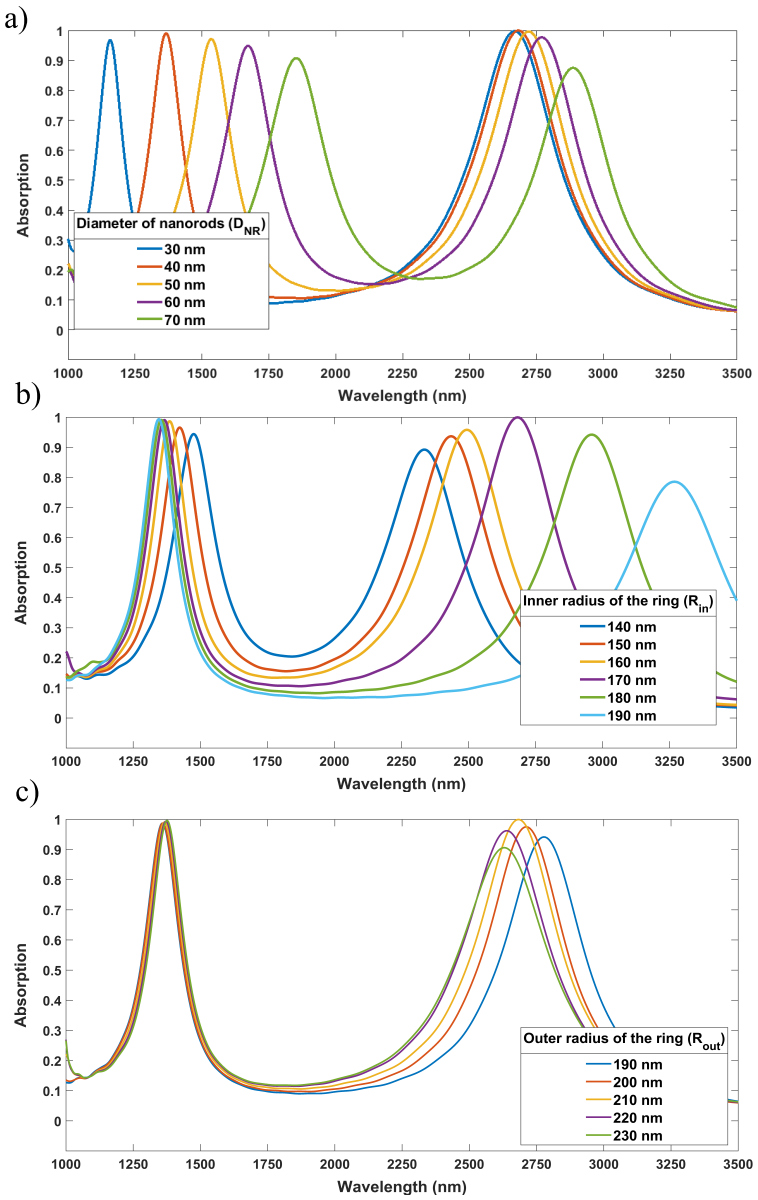


**Fig. 6.** Change in absorption spectra in response to the change in a) diameter of nanorods ($D_{NR}$), b) Inner radius of the ring ($R_{IN}$), c) Outer radius of the ring ($R_{OUT}$).

With the altering values of the polarization angle of the incident light, the localized electric field profile in the structure remains constant; thereby the locations of the resonances and the amount of absorption stayed almost unchanged. This consistency is attributed to the highly symmetrical configuration of the proposed structure. Figure 7 shows the absorption spectra of the absorber when illuminated by incident light with different polarization angles individually. As the polarization angle varies from 0° to 90°, the position of $M_1$ shifts from 1366 nm to 1400

OPTICS CONTINUUM

nm, while $M_2$ shows almost no change as it is associated with the ring of the nanostructure, which has complete radial symmetry and remains unaffected irrespective of the polarization angle.

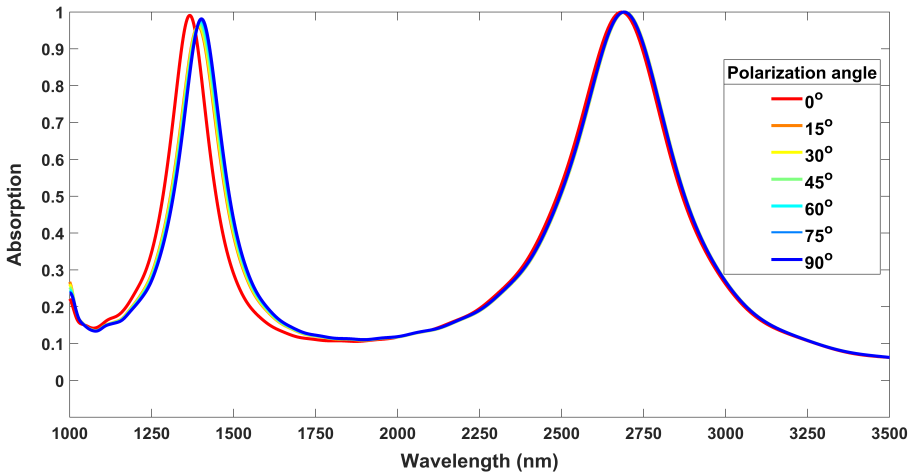


**Fig. 7.** Absorption spectra obtained for various polarization angles of the normally incident light.

The response of the absorber shown in Fig. (2–7) is calculated considering surface-normal incidence of the light. In practice, this can be implemented using an appropriate setup (for instance, mounting the sensor on a translation stage and collimators [57]). Nevertheless, we also examined the structure's behavior under light at various incident angles rather than at normal incidence (detailed results are provided in the Supplement 1). The resonance wavelengths for both modes remain unchanged regardless of the incident angle, as does the absorption rate. Reflectance fluctuates slightly at non-resonance frequencies for larger incident angles, which can be conveniently resolved by ensuring that the light illuminates the absorber at angles less than 25°by employing similar experimental configurations as referenced earlier.

### *4.1. Sensing performance*

To assess the sensing performance of our introduced absorber as a refractive index sensor, first, we calculated the refractive index sensitivity (*RIS*). Refractive index sensitivity is a key and widely utilized parameter for assessing a sensor's performance. It measures how the sensor's resonance wavelength responds to changes in the bulk refractive index of the environment in which it operates and can be expressed through the equation below [58],

$$RIS = \frac{\Delta\lambda_{\text{res}}}{\Delta n}. \tag{4}$$

Here, $\Delta n$ represents the change in refractive index, while $\Delta\lambda_{\text{res}}$ denotes the corresponding change in resonance wavelength.

We adjusted the refractive index of the sensor's surrounding environment from 1.0 to 2.0 in increments of 0.1 and determined the resonance wavelengths for both modes individually for each instance as shown in Fig. 8(a), and (b). Additionally, we considered the values of the refractive index from 1.33 to 1.36 with a step size of 0.005, since analytes in biosensing applications typically have a refractive index within this range (e.g., blood plasma 1.34, glucose in water 1.33–1.36, E. coli in food samples 1.344–1.347; Supplement 1 for details) [59,60]. Analyzing the data obtained from these simulations, we found the RIS value for M1 to be 828 nm/RIU, and that for M2 to be 1550 nm/RIU, which is satisfactorily high for biosensing and chemical sensing

OPTICS CONTINUUM

purposes. A linear redshifting trend of the resonance wavelengths can also be noticed in Fig. 8(a) and (b).

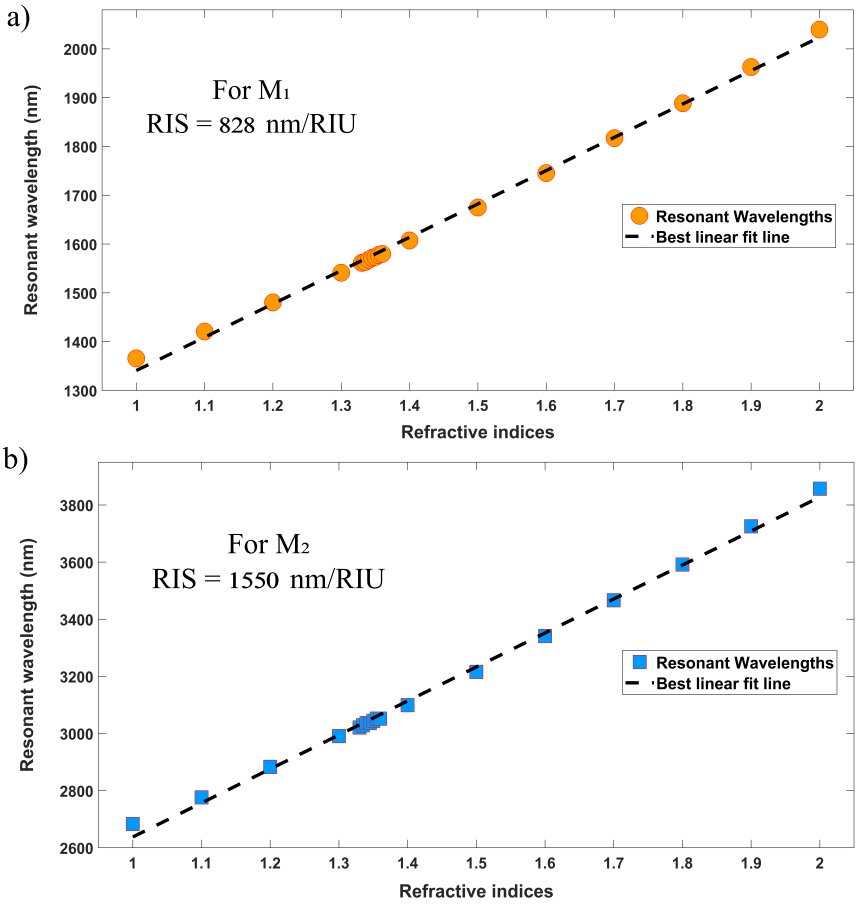


**Fig. 8.** The resonant wavelengths of the two modes exhibit a linear trend in shifting as they change with the effective refractive index of the surrounding environment a) for $M_1$, b) for $M_2$

We also computed the figure of merit of our absorber in sensing tasks considering both $M_1$ and $M_2$. The figure of merit ($FoM$) standardizes the bulk refractive index sensitivity ($RIS$) by relating it to the resonance curve's width, defined by the full width at half maximum ($FWHM$), which determines the accuracy of measuring the resonance minimum [58].

$$FoM = \frac{RIS}{FWHM}. \tag{5}$$

The equation above that describes FoM was utilized to calculate the values of FoM, and the obtained values are 6.3 per RIU and 5.9 per RIU for $M_1$ and $M_2$, respectively.

### 4.2. Comparison with literature

We compared the evaluated sensing performance with previously reported dual or multi-band absorbers, as shown in Table 1.

In comparison to previous studies, it is evident that the absorber introduced in this study exhibits dual-band high absorption, a high $RIS$ value, and an acceptable $FoM$ while offering the

OPTICS CONTINUUM

**Table 1. Comparison with dual/multi-band sensors reported in recent years**

| Reference | Resonant wavelengths | Operating band | $RIS_{max}$ (for all peaks, respectively) [nm/RIU] | *FoM* (for all peaks, respectively) [/RIU] |
|---|---|---|---|---|
| [61] | 870 nm, 1599 nm | Only near-infrared | 365, 733 | 12, 10.4 |
| [62] | 896 nm, 1471 nm | Only near-infrared | 585.27, 652.77 | 6.88, 4.21 |
| [39] | 727 nm, 1000 nm | Only near-infrared | 1000, 650 | 10.0, 8.13 |
| [38] | 1500 nm, 1720 nm | Only near-infrared | 800, 1240.8 | 44.5, 40.5 |
| [63] | 3.27 μm - 4.5 μm | Only mid-infrared | 666.75 - 907.88 | 86.82 - 56.14 |
| [64] | 3.4 μm - 4.3 μm | Only mid-infrared | 635.75 - 839.39 | 54.03 - 52.14 |
| This work | 1366 nm, 2683 nm | Both near-infrared and mid-infrared | 828, 1550 | 6.3, 5.9 |

advantages of two working windows in two distinct IR regions and the flexibility to select desired operating wavelengths in both the NIR and MIR bands simultaneously, thereby broadening its potential range of applications.

### 4.3. Applications

To examine the compatibility of our proposed absorber as a sensor in the field of biosensing and environment monitoring, we incorporated it into diverse sensing scenarios. By applying the principle of refractive index sensing, we simulated its use for detecting gas hydrates, identifying various proteins at different concentrations dissolved in water, distinguishing amino acids from their isomers, and determining concentrations of various inorganic and organic solutes in aqueous solutions to assess its performance as a chemical sensor. Additionally, to investigate its potential as a biosensor, we simulated its application in detecting E. coli in food and beverage samples, quantifying biomolecule attachment on its surface, measuring hemoglobin concentration in human blood, confirming DNA hybridization completion, and detecting various viruses. Detailed results and discussions are provided in the Supplement 1 article.

## 5. Conclusion

In summary, the dual-band plasmonic absorber we presented in this letter exhibits high sensitivity across both the NIR and MIR regions with one absorption peak at 1366 nm with 99.5% absorption and another peak with 99.99% absorption at 2683 nm, offering the potential for various sensing applications such as biomolecule detection, virus identification, and environmental monitoring. The structure's ability to achieve a high refractive index sensitivity of 1550 nm/RIU and a moderately high FoM of 6.3 per RIU, along with its compact design, tolerance to potential fabrication imperfection, the polarization of incident light, and compatibility with a broad range of analytes, implies its promise for advanced sensing technologies. The absorber's performance is enhanced by combining localized and gap surface plasmon resonances, leading to significant shifts in resonance wavelengths with changes in the surrounding environment. Looking forward, incorporating additional materials such as graphene and further engineering its

OPTICS CONTINUUM

intrinsic parameters may significantly enhance the performance of the structure, paving the way for the development of advanced sensing technologies.

**Disclosures.** The authors declare no conflicts of interest.

**Data availability.** Data will be made available upon request.

**Supplemental document.** See Supplement 1 for supporting content.

## References


1. M. I. Stockman, K. Kneipp, S. I. Bozhevolnyi, *et al.*, "Roadmap on plasmonics," J. Opt. **20**(4), 043001 (2018).
2. Q. Duan, Y. Liu, S. Chang, *et al.*, "Surface plasmonic sensors: Sensing mechanism and recent applications," Sensors **21**(16), 5262 (2021).
3. C. Lee, B. Lawrie, R. Pooser, *et al.*, "Quantum plasmonic sensors," Chem. Rev. **121**(8), 4743–4804 (2021).
4. J. Divya, S. Selvendran, A. S. Raja, *et al.*, "Surface plasmon based plasmonic sensors: A review on their past, present and future," Biosens. Bioelectron.: X **11**, 100175 (2022).
5. M. A. Butt, "Insight into plasmonics: resurrection of modern-day science," Comput. Opt. **48**(1), 5–17 (2024).
6. A. Ghobadi, ""strong light-matter interaction in lithography-free perfect absorbers for photoconversion, photodetection, light emission, sensing, and filtering applications," Ph.D. thesis, Bilkent Universitesi (Turkey) (2022).
7. W. Aroua, J. Derbali, M. Raaif, *et al.*, "Ultrasensitive plasmonic biosensor based on metal/porous graphene/perovskite multilayers," Opt. Mater. **153**, 115613 (2024).
8. B. Kaur, A. K. Sharma, and Y. Prajapati, "Plasmonic sensor for magnetic field detection with chalcogenide glass and ferrofluid materials under thermal variation in near infrared," Opt. Mater. **117**, 111175 (2021).
9. M. Berka, B. Fellah, S. Das, *et al.*, "Nano-resonator based broadband metamaterial absorber with angular stability operating in visible light spectrum for solar energy harvesting applications," Opt. Mater. **149**, 115043 (2024).
10. Y. Li, Q. Liao, W. Hou, *et al.*, "Silver-based surface plasmon sensors: fabrication and applications," Int. J. Mol. Sci. **24**(4), 4142 (2023).
11. V. Sudarsan, "Optical materials: fundamentals and applications," Functional Materials: Preparation, Processing and Applications pp. 285–322 (2012).
12. Y. H. Jang, Y. J. Jang, S. Kim, *et al.*, "Plasmonic solar cells: from rational design to mechanism overview," Chem. Rev. **116**(24), 14982–15034 (2016).
13. R. P. Kooyman, "Physics of surface plasmon resonance," in *Handbook of Surface Plasmon Resonance*, (The Royal Society of Chemistry, 2008).
14. L. Du, X. Zhang, T. Mei, *et al.*, "Localized surface plasmons, surface plasmon polaritons, and their coupling in 2d metallic array for sers," Opt. Express **18**(3), 1959–1965 (2010).
15. W. X. Tang, H. C. Zhang, H. F. Ma, *et al.*, "Concept, theory, design, and applications of spoof surface plasmon polaritons at microwave frequencies," Adv. Opt. Mater. **7**(1), 1800421 (2019).
16. S. J. Zalyubovskiy, M. Bogdanova, A. Deinega, *et al.*, "Theoretical limit of localized surface plasmon resonance sensitivity to local refractive index change and its comparison to conventional surface plasmon resonance sensor," J. Opt. Soc. Am. A **29**(6), 994–1002 (2012).
17. X. Rao, H. Zhu, X. Wang, *et al.*, "Self-referential plasmonic refractive index sensor by square hole array and gold film coupling structure," Plasmonics **20**, 2187–2196 (2024).
18. S. Hu, W. Shi, Y. Chen, *et al.*, "Universal and flexible design for high-sensitivity and wide-ranging surface plasmon resonance sensors based on a three-dimensional tuning hypersurface," Sens. Actuators, B **380**, 133284 (2023).
19. A. A. Dormeny, P. A. Sohi, and M. Kahrizi, "Design and simulation of a refractive index sensor based on spr and lspr using gold nanostructures," Results Phys. **16**, 102869 (2020).
20. P. Singh, V. Singh, and S. Chualya, "Numerical analysis of lspr based fiber sensor for low refractive index detection," Optik **224**, 165704 (2020).
21. J. Jatschka, A. Dathe, A. Csáki, *et al.*, "Propagating and localized surface plasmon resonance sensing—a critical comparison based on measurements and theory," Sens. Bio-Sens. Res. **7**, 62–70 (2016).
22. Y. Min and Y. Wang, "Manipulating bimetallic nanostructures with tunable localized surface plasmon resonance and their applications for sensing," Front. Chem. **8**, 411 (2020).
23. H. Wang, T. Wang, S. Zhong, *et al.*, "Sensitivity investigation of a biosensor with resonant coupling of propagating surface plasmons to localized surface plasmons in the near infrared region," Nanoscale **15**(25), 10826–10833 (2023).
24. P. T. Dang, T. V. Vu, J. Kim, *et al.*, "Efficient broadband truncated-pyramid-based metamaterial absorber in the visible and near-infrared regions," Crystals **10**(9), 784 (2020).
25. H. Liu, X. Sun, F. Yao, *et al.*, "Controllable coupling of localized and propagating surface plasmons to tamm plasmons," Plasmonics **7**(4), 749–754 (2012).
26. A. Farhang, N. Bigler, and O. J. Martin, "Coupling of multiple lsp and spp resonances: interactions between an elongated nanoparticle and a thin metallic film," Opt. Lett. **38**(22), 4758–4761 (2013).
27. S. S. Bukhari, J. Vardaxoglou, and W. Whittow, "A metasurfaces review: Definitions and applications," Appl. Sci. **9**(13), 2727 (2019).
28. Y.-F. Chou Chau, T. Y. Ming, C.-T. Chou Chao, *et al.*, "Significantly enhanced coupling effect and gap plasmon resonance in a mim-cavity based sensing structure," Sci. Rep. **11**(1), 18515 (2021).

OPTICS CONTINUUM


29. Y.-F. Chou Chau, C.-T. Chou Chau, H. J. Huang, *et al.*, "Perfect dual-band absorber based on plasmonic effect with the cross-hair/nanorod combination," Nanomaterials **10**(3), 493 (2020).
30. Y. Liang, X. Liu, J. Xin, *et al.*, "Ultra-broadband long-wave infrared metasurface absorber based on peano fractal curve," Results Phys. **33**, 105169 (2022).
31. Y. Zhong, S. D. Malagari, T. Hamilton, *et al.*, "Review of mid-infrared plasmonic materials," J. Nanophotonics **9**(1), 093791 (2015).
32. C. Sandorfy, R. Buchet, and G. Lachenal, "Principles of molecular vibrations for near-infrared spectroscopy," *Near-Infrared Spectroscopy in Food Science and Technology*; Y. Ozaki, W. F. McClure, and A. A. Christy, eds., pp. 11–46 (2007).
33. T. G. Mayerhöfer, S. Pahlow, and J. Popp, "Recent technological and scientific developments concerning the use of infrared spectroscopy for point-of-care applications," Spectrochimica Acta Part A: Mol. Biomol. Spectrosc. **251**, 119411 (2021).
34. M. El-Azazy, A. S. El-Shafie, and K. Al-Saad, "Introductory chapter: infrared spectroscopy-principles and applications," in *Infrared Spectroscopy-Perspectives and Applications*, (IntechOpen, 2023).
35. M. Manley, "Near-infrared spectroscopy and hyperspectral imaging: non-destructive analysis of biological materials," Chem. Soc. Rev. **43**(24), 8200–8214 (2014).
36. S. De Bruyne, M. M. Speeckaert, and J. R. Delanghe, "Applications of mid-infrared spectroscopy in the clinical laboratory setting," Crit. Rev. Clin. Lab. Sci. **55**(1), 1–20 (2018).
37. B. Khodadadi, P. Rezaei, and S. Hadipour, "Dual-band polarization-independent maze-shaped absorber based on graphene for terahertz biomedical sensing," Opt. Express **33**(3), 3869–3880 (2025).
38. A. Alipour, A. Mir, and A. Farmani, "Ultra high-sensitivity and tunable dual-band perfect absorber as a plasmonic sensor," Opt. & Laser Technol. **127**, 106201 (2020).
39. C.-T. Chou Chao, Y.-F. Chou Chau, and H.-P. Chiang, "Biosensing on a plasmonic dual-band perfect absorber using intersection nanostructure," ACS Omega **7**(1), 1139–1149 (2022).
40. Y. Cheng, H. Zhang, X. S. Mao, *et al.*, "Dual-band plasmonic perfect absorber based on all-metal nanostructure for refractive index sensing application," Mater. Lett. **219**, 123–126 (2018).
41. K. Chen, R. Adato, and H. Altug, "Dual-band perfect absorber for multispectral plasmon-enhanced infrared spectroscopy," ACS Nano **6**(9), 7998–8006 (2012).
42. L. Zhang, W. Lu, L. Zhu, *et al.*, "Dual-band complementary metamaterial perfect absorber for multispectral molecular sensing," Opt. Express **31**(19), 31024–31038 (2023).
43. X.-Y. Chen, K. Yu, S.-W. Zheng, *et al.*, "Dual-band, high sensitivity, angle-insensitive graphene—perfect absorber based on surface plasmon resonance," Diamond Relat. Mater. **142**, 110728 (2024).
44. W. Shen, T. Hu, X. Liu, *et al.*, "Defect engineering of layered double hydroxide nanosheets as inorganic photosensitizers for nir-iii photodynamic cancer therapy," Nat. Commun. **13**(1), 3384 (2022).
45. J. Workman Jr, "A brief review of near infrared in petroleum product analysis," J. Near Infrared Spectrosc. **4**(1), 69–74 (1996).
46. F. Yang, Q. Zhang, S. Huang, *et al.*, "Recent advances of near infrared inorganic fluorescent probes for biomedical applications," J. Mater. Chem. B **8**(35), 7856–7879 (2020).
47. L. A. Sordillo, Y. Pu, S. Pratavieira, *et al.*, "Deep optical imaging of tissue using the second and third near-infrared spectral windows," J. Biomed. Opt. **19**(5), 056004 (2014).
48. A. Boltasseva and H. A. Atwater, "Low-loss plasmonic metamaterials," Science **331**(6015), 290–291 (2011).
49. X. Wu, Y. Zheng, Y. Luo, *et al.*, "A four-band and polarization-independent bds-based tunable absorber with high refractive index sensitivity," Phys. Chem. Chem. Phys. **23**(47), 26864–26873 (2021).
50. N. Singh and P. Khanna, "In situ synthesis of silver nano-particles in polymethylmethacrylate," Mater. Chem. Phys. **104**(2-3), 367–372 (2007).
51. M. Kazemian Abyaneh, S. Jafarkhani, and S. Kulkarni, "Electrical transport behaviour of silver–pmma nanocomposite films at low temperature," J. Exp. Nanosci. **6**(2), 159–173 (2011).
52. E. D. Palik, *Handbook of optical constants of solids*, vol. 3 (Academic press, 1998).
53. R. Paschotta, *et al.*, *Encyclopedia of laser physics and technology*, vol. 1 (Wiley Online Library, 2008).
54. M. N. Polyanskiy, "Refractiveindex. info database of optical constants," Sci. Data **11**(1), 94 (2024).
55. F. Ding, Y. Yang, R. A. Deshpande, *et al.*, "A review of gap-surface plasmon metasurfaces: fundamentals and applications," Nanophotonics **7**(6), 1129–1156 (2018).
56. N. J. Halas, S. Lal, W.-S. Chang, *et al.*, "Plasmons in strongly coupled metallic nanostructures," Chem. Rev. **111**(6), 3913–3961 (2011).
57. Y. Liu, S. Wang, P. Biswas, *et al.*, "Optofluidic vapor sensing with free-space coupled 2d photonic crystal slabs," Sci. Rep. **9**(1), 4209 (2019).
58. Y. Xu, P. Bai, X. Zhou, *et al.*, "Optical refractive index sensors with plasmonic and photonic structures: promising and inconvenient truth," Adv. Opt. Mater. **7**(9), 1801433 (2019).
59. W. Wang, Z. Mai, Y. Chen, *et al.*, "A label-free fiber optic spr biosensor for specific detection of c-reactive protein," Sci. Rep. **7**(1), 16904 (2017).
60. J. Li, "A review: Development of novel fiber-optic platforms for bulk and surface refractive index sensing applications," Sens. Actuators Rep. **2**(1), 100018 (2020).

OPTICS CONTINUUM

61. T. Zahra, M. A. Mohemine, A. A. Syed, *et al.*, "Design and performance of a dual-band plasmonic perfect absorber for infrared refractive index sensing," Appl. Opt. **63**(29), 7796–7801 (2024).
62. Z. Madadi, K. Abedi, G. Darvish, *et al.*, "Dual-wavelength plasmonic perfect absorber suitable for refractive index sensing," Plasmonics **15**(3), 703–708 (2020).
63. Z. Chen, H. Chen, J. Yin, *et al.*, "Multi-band, tunable, high figure of merit, high sensitivity single-layer patterned graphene—perfect absorber based on surface plasmon resonance," Diamond Relat. Mater. **116**, 108393 (2021).
64. H. Chen, Z. Chen, H. Yang, *et al.*, "Multi-mode surface plasmon resonance absorber based on dart-type single-layer graphene," RSC Adv. **12**(13), 7821–7829 (2022).